JOURNAL OF MATERIALS SCIENCE 28 (1993) 2217–2226

Microstructural and magnetic characterization of alumina–iron nanocomposites

A. MARCHAND, X. DEVAUX, B. BARBARA, P. MOLLARD, M. BRIEU, A. ROUSSET
Laboratoire de Magnétisme Louis Néel, CNRS BP 166, 38042 Grenoble Cedex 9, France
Laboratoire de Chimie des Matériaux Inorganiques, URA-CNRS 1311, Université Paul Sabatier, 31062 Toulouse Cedex, France

Iron–alumina nanocomposite powders containing 10 wt % iron were prepared by selective reduction of alumina–haematite solid solutions. Microstructural study showed three types of metal dispersion in the alumina matrix according to the elaboration process: iron grains that were > 70 nm, most of the iron particles were < 10 nm and directly epitaxied in the alumina matrix, and iron particles that were surrounded by an interfacial phase. In agreement with transmission electron miscroscopy (TEM) observations, magnetic study confirmed a distribution of the iron particles size, showing the superposition of a ferromagnetic behaviour (larger particles) and a superantiferromagnetic behaviour (smaller particles). Furthermore, analysis of thermoremanent behaviour, coercive field and dissymmetry of hysteresis loops allowed the interfacial phase surrounding some iron particles to be identified as an antiferromagnetic phase, $Fe_{1+x}Al_{2-x}O_4$. Nevertheless, at the interface of metallic iron epitaxied on the alumina matrix some atomic planes always existed where iron was ionic (even if no other phase was detected). As a consequence the mean magnetic moment of iron in these nanocrystals is larger than that in bulk metallic iron.

1. Introduction

In 1949 Néel [1, 2] pointed out that fine ferromagnetic particles may present a particular magnetic state: superparamagnetism [3]. A rough estimate of the maximum radius for a spherical sample of common ferromagnetic materials is about 15 nm [4]. These nanoparticles are single magnetic domains. In nature, single-domain particles are not completely isotropic in their properties, but will have anisotropic contributions to their energy arising from the external shape of the nanoparticle, imposed stresses or the crystalline structure itself. The magnetic moments of nanoparticles orient themself in the direction of the easy magnetization axis, but thermal energy at the experimental temperature causes passage on other easy magnetization directions. Then there is relaxation of magnetic moments between the different easy magnetization directions. If the time necessary for magnetic measurement is greater than this relaxation time, then the experimenter will observe a disordered magnetic state similar to paramagnetism. However, here the difference is that the paramagnetic relaxation times are much larger than those of atomic moments. This "superparamagnetic" state will be observed only from a sufficiently high temperature, when relaxation by thermal energy kT is larger than the anisotropy energy KV. The temperature, T_B, for which $kT_B \approx KV$, called the blocking temperature, is obviously a function of the particle size. The blocking temperature weakens as the size decreases. Magnetic properties such as the coercive field, remanent magnetization, isothermal magnetization versus applied field and d.c. and a.c. susceptibilities will be modified strongly in comparison with bulk material magnetic properties. Reviews of superparamagnetism and associated phenomena are given in [5, 6].

Superparamagnetism has found applications in many studies related to problems in catalysis: formation of nickel particles supported on silica and adsorbed gases on nickel catalysts. A review of these works is given in [7], bringing to the fore two states of chemisorption of hydrogen on supported nickel catalysts [8] and magnetization measurements leading to crystallite size distributions of dispersed nickel [9].

The study of magnetism at surfaces and interfaces has been strongly developed in recent years. Much of this experimental and theoretical effort has been addressed to transition metals (Cr, Fe, V and Ni) and noble metals (Cu, Ag and Au) which have a microstructure of nanometre scale: nanoparticles, surfaces and interfaces, and modulated structures [10]. The existence of surface and interface states, the reduced co-ordination number and the symmetry of atoms in the surface layer lead to important differences with respect to the bulk system, and would give new information on the electronic structure and magnetic properties of these materials [11–13]. New theories estimate, in the cases of nanolayers of Fe adsorbed on

Ag (0 0 1) [10], of a seven-layer Fe (0 0 1) thin film [13] and of clusters of Fe_n ($n \leqslant 15$) [14], that iron exists in these structures with a magnetic moment 20–40% greater than that of bulk iron.

In chromium single-crystal particles from 38 to 75 nm in diameter [15] a new magnetic transition was observed at about 800 K instead of 310 K. This magnetic phase would be due to magnetic order localized near the surface.

2. Specimens preparation and experimental procedure

Synthesis of alumina–iron nanocomposite powders was obtained by selective reduction of alumina–haematite solid solutions. A description of the chemical preparation was published elsewhere [16]. Four types of specimens were selected according to the preparation. For a ratio Fe/(Fe + Al) = 0.10:

specimens A: iron particles with a large mean diameter, about 80 nm;

specimens B: iron nanoparticles with a small mean diameter, about 5 nm, surrounded by an iron aluminate shell;

specimens C: iron nanoparticles, 5 nm average diameter, directly epitaxied in the alumina matrix; and

specimens D: elaborated from specimens B by heating under hydrogen (800 °C for 50 h); the iron aluminate shell disappeared and the iron particles were epitaxied in alumina.

For a ratio Fe/(Fe + Al) = 0.05 a specimen B (called B 5%) was also prepared for the study of coercive fields and thermoremanence.

These different specimens were very carefully analysed by atomic absorption spectrometry (AAS) at Service Central d'Analyse du CNRS (France). X-ray diffraction (XRD) analysis was realized with a Siemens D 501 powder diffractometer using CoK_α radiation ($\lambda = 0.179\,025$ nm). The microstructures of alumina–iron composites were studied in a Jeol 200 CX TEM.

Magnetic measurements were performed in a conventional magnetometer providing a magnetic field up to 7 T and temperature from 1.5 to 300 K. Some measurements were realized at 4.2 K with magnetic field up to 20 T at the Service National des Champs Intenses (Max Planck Institute, Grenoble). The magnetic measurements also involved isothermal magnetization versus applied magnetic field, and the determination of thermoremanence, coercive field and thermomagnetic evolution.

3. Results

3.1. X-ray crystallography studies

Results of AAS and XRD analyses are given in Table I. Chemical quantitative analysis could not detect the existence of any element other than Fe, Al and O with a rate greater than 50 p.p.m. Moreover, we note that the four specimens contained the same iron concentration.

Fig. 1 shows that only α-Al_2O_3 γ-Al_2O_3 and α-Fe were detected in the XRD patterns. γ-Al_2O_3 was present in specimen A only, and in low concentration. The width and weak intensity of the iron peak in specimens B, C and D was due to the small metal particles size (Table II). The lattice parameter value of the corundum phase seems to indicate that haematite was totally reduced into iron during the preparation of the nanocomposite powders.

3.2. Microstructural studies of the nanocomposites

The specimens microstructures are shown in Figs 2–5. In the bright-field micrographs (Figs 2, 3, 4a and 5a) the iron appears as single-crystal particles dispersed in the α-alumina matrix. Table II gives the average size of the iron particles, calculated by measurements of 1000 particles on TEM micrographs.

TABLE I Crystallographical and chemical characteristics of alumina–iron nanocomposite powders

Specimen	Fe/(Fe + Al) by AAS (at %)	Fe weight as percentage initial weight (at %)	Phases detected by XRD
A	10.0	10.7	α-Al_2O_3 + γ-Al_2O_3 + α-Fe
B	10.0	10.7	α-Al_2O_3 + α-Fe
C	10.0	10.7	α-Al_2O_3 + α-Fe
D	10.0	10.7	α-Al_2O_3 + α-Fe

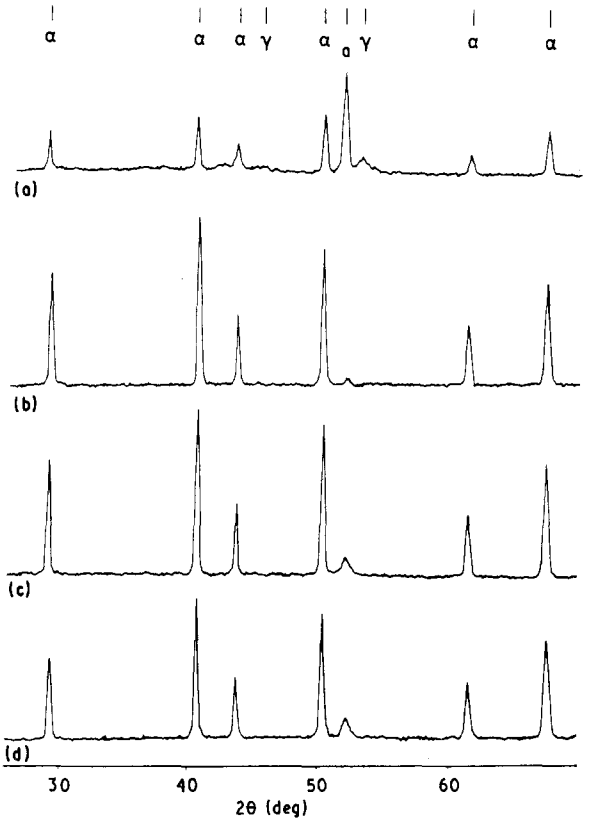

Figure 1 XRD patterns for specimens (a) A, (b) B, (c) C and (d) D: peaks α, α-Al_2O_3; γ, γ-Al_2O_3; α, α-Fe.

TABLE II Average size of metal particles dispersed in alumina

Specimen	$\bar{d}$ by TEM (nm)	$\bar{d}$ by XRD (nm)
A	80	75
B	10	Weak intensity
C	5	Weak intensity
D	5	Weak intensity

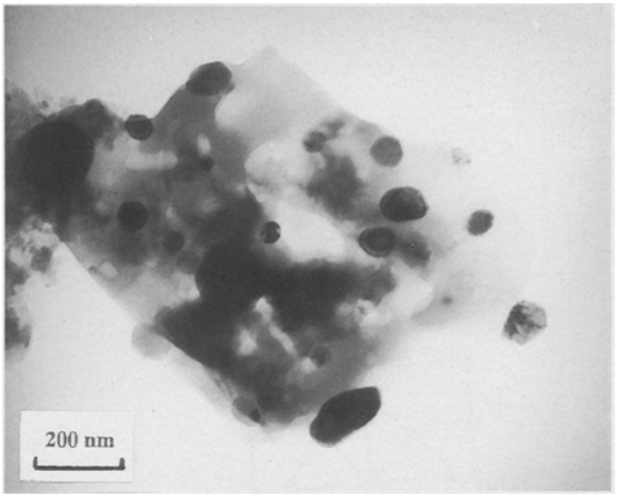

Figure 2 Bright-field TEM micrograph of specimen A.

For specimen A the iron crystallite size (Fig. 2) is between 50 and 100 nm. The average value (80 nm) is in good agreement with that obtained from XRD patterns analysis by Scherrer's method. For specimens B, C and D the figures show that the average size of the iron particles was much smaller: diameters spread between 1 and 20 nm. These results confirm the previous hypothesis that the weak intensity and width of the iron XRD peaks are due to the small size of these particles. However, we remark that for specimen B (Fig. 3) each iron particle was surrounded by a phase with a contrast different from that of alumina or iron. The thickness of these interfacial phases was between 2 and 3 nm. The Fe–Al–O phase diagram, from the works of Imlach and Glasser [17] on the reduction of polluted magnetite by alumina and those of Ogale *et al.* [18] on the structure and chemistry of ceramic–metal interfaces, allow us to think that the interfacial phase might be a spinel $Fe_{1+x}\,Al_{2-x}\,O_4$.

Fig. 4b shows the electron microdiffraction pattern of specimen C. Analysis of this diffraction diagram (Fig. 6) showed that the whole batch of iron particles contained in an alumina single-crystal line grain behave as a single crystal. This behaviour shows that all the iron particles in specimen C were epitaxied in alumina and therefore had the same crystallographic orientation. The dark-field micrograph in Fig. 4c was obtained with electron beams diffracted by $(2\bar{1}0)$ alumina planes. This micrograph shows that the alumina grain studied was a single crystal. A comparison between the bright-field (Fig. 4a) and dark-field made with the beams diffracted by the α-Fe (1 0 1) planes (Fig. 4d) revealed that all iron particles had the same

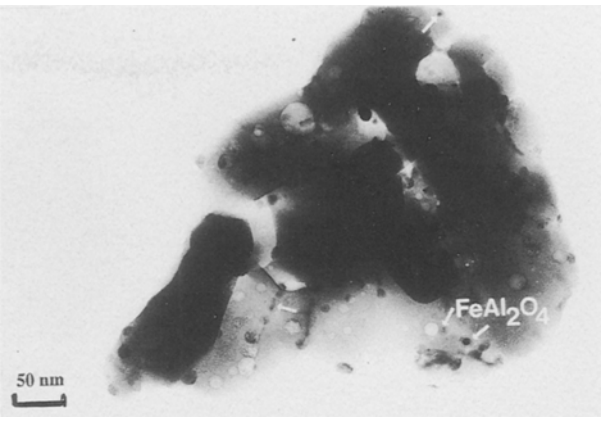

Figure 3 Bright-field TEM micrograph of specimen B.

crystallographic orientation. From these micrographs the following orientation relationships between the alumina lattice and iron lattice are deduced:

$$(1\,0\,\bar{1})_{\alpha\text{-Fe}} \| (2\,\bar{1}\,0)_{\alpha\text{-}Al_2O_3}$$
$$(1\,0\,1)_{\alpha\text{-Fe}} \| (0\,\bar{1}\,4)_{\alpha\text{-}Al_2O_3}$$
$$(1\,0\,0)_{\alpha\text{-Fe}} \| (1\,\bar{1}\,2)_{\alpha\text{-}Al_2O_3}$$
$$(0\,0\,1)_{\alpha\text{-Fe}} \| (\bar{1}\,0\,2)_{\alpha\text{-}Al_2O_3}$$

This is summarized by the epitaxial relationship

$$(1\,1\,1)\,[(\bar{1}\,\bar{1}\,2)]_{\alpha\text{-Fe}} \| (0\,0\,1)\,[(2\,1\,0)]_{\alpha\text{-}Al_2O_3}$$

Other authors have observed the same orientation for body-centred cubic metals epitaxied in α-alumina. Anton *et al.* [19] observed the parallelism of iron (1 1 0) and α-Al_2O_3 (1 1 0) planes in iron thin films on a sapphire substrate, and Qadri *et al.* [20] demonstrated that niobium is epitaxied in alumina according to $(1\,1\,1)_{Nb} \| (0\,0\,1)_{\alpha\text{-}Al_2O_3}$.

In an attempt to see the influence of the iron aluminate interfacial shell, detected in specimen B, on the microstructural and magnetic properties of the iron dispersed in alumina, we performed a reduction of specimen B, in order to reduce the Fe^{2+} ions contained in iron aluminate. The bright-field micrograph in Fig. 5a shows that the iron aluminate interfacial shell around iron particles in specimen B had disappeared. Analysis of the electron microdiffraction pattern (Fig. 5b) gave the same crystallographic relationship between iron and alumina as observed in specimen C.

3.3. Studies of magnetic properties

3.3.1. Isothermal magnetization curves

These curves were measured for the four specimens A, B, C and D for which microstructural properties were described in section 3.2.

3.3.1.1. Specimen A (Fig. 7). This specimen was essentially characterized by iron particles of large diameter (between 50 and 100 nm) with a small distance between each other. The distance between the particle

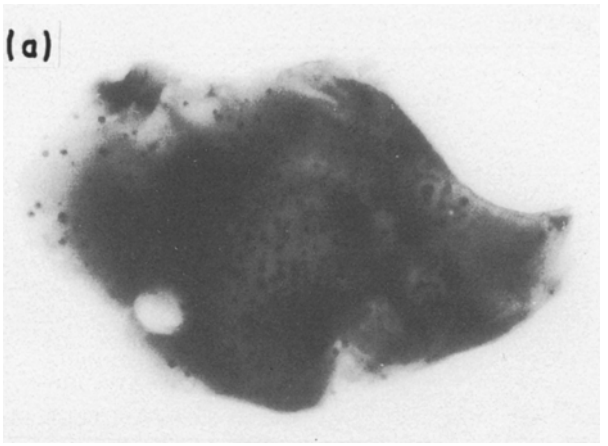

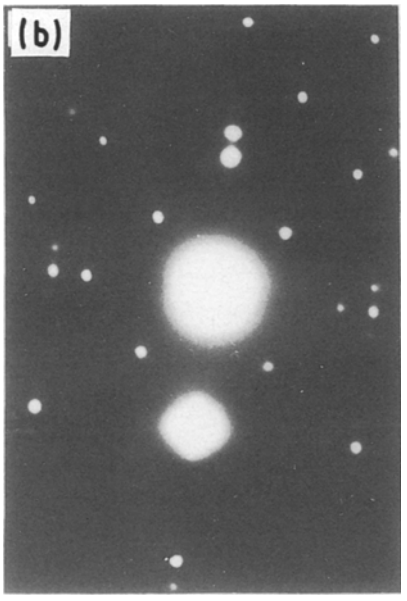

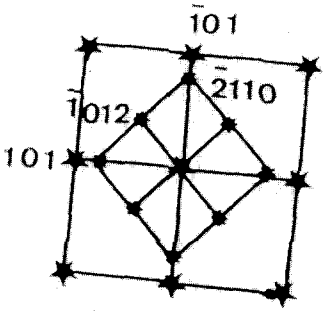

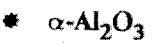

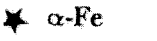

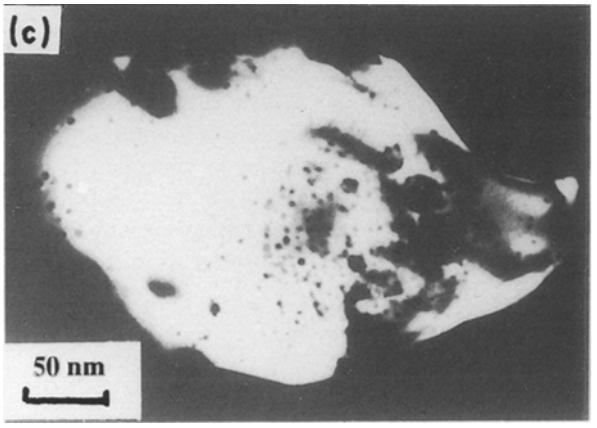

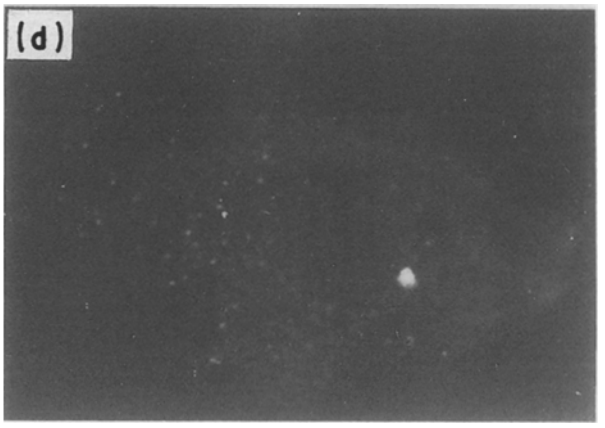

Figure 4 TEM micrographs of specimen C: (a) bright-field, (b) electron microdiffraction pattern, (c) dark-field of alumina grain and (d) dark-field of iron particles.

centres is in the range 120–160 nm. The magnetization curves versus temperature do not vary from 1.5 to 300 K, which means that the Curie temperature is still high in these particles. These curves show a very fast variation of the magnetization in weak magnetic fields; this variation, practically linear, recalls a demagnetizing field straight line. The single domain state will be obtained for a magnetic field of about 8 kOe (1 Oe $\approx$ 79.58 A m^{-1}), which gives an average demagnetizing field coefficient of about 4, near to that of a sphere.

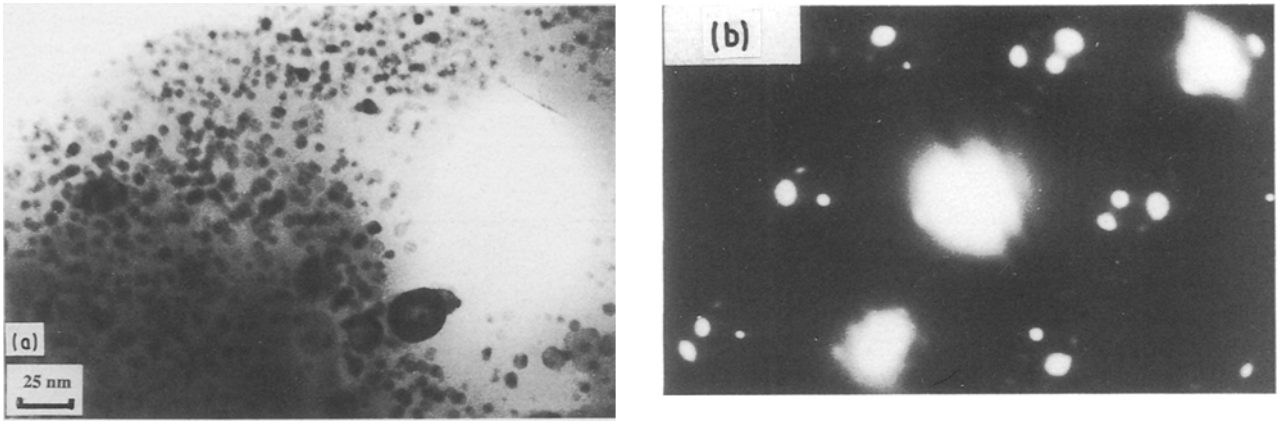

Figure 5 (a) TEM micrograph and (b) electron microdiffraction pattern of specimen D.

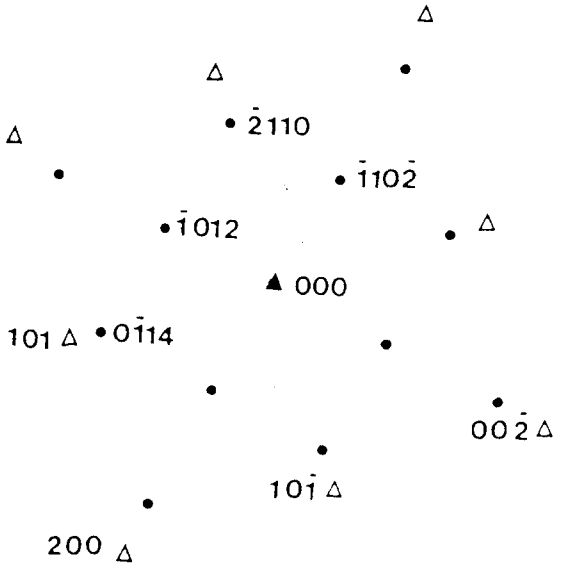

Figure 6 Electron microdiffraction pattern for specimen C: (△) α-Fe and (●) α-Al_2O_3.

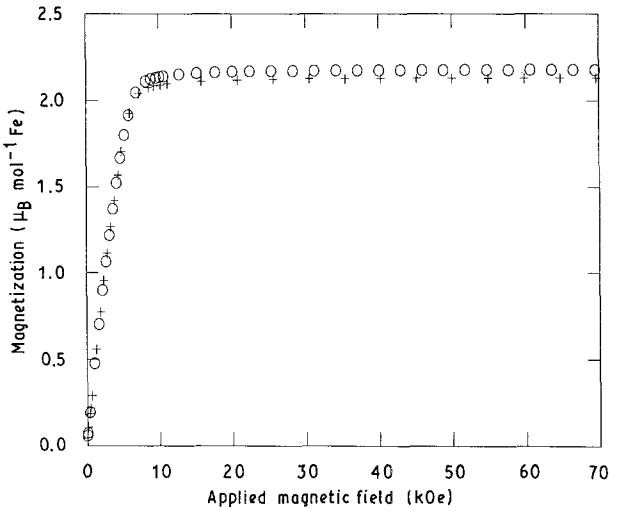

Figure 7 Isothermal magnetization versus applied magnetic field curves for specimen A: (○) 1.5 K and (+) 300 K. 1 Oe ≈ 79.58 A m^{-1}; 1 $\mu_B \approx 9.27 \times 10^{-24}$ J T^{-1}.

When the magnetic field is strong, the magnetization varies linearly with the field. The susceptibility is weak, about 5.48×10^{-4} e.m.u. mol^{-1} iron, this value is slightly larger than those given for bulk Fe specimens (2.66×10^{-4} [21], 2.31×10^{-4} [22] and 3.05×10^{-4} [23]). The spontaneous magnetization is obtained by the intersection of the two linear variations: the low-field straight line of the demagnetizing field regime, and the large field magnetization curve of the saturation regime. For example we obtain 2.174 μ_B at 1.5 K and 2.122 μ_B at 300 K (1 $\mu_B \approx 9.27 \times 10^{-24}$ J T^{-1}). The total variation obtained from 1.5 to 300 K is shown in Fig. 11 (below). These values are very close to those of bulk iron.

3.3.1.2. Specimens B, C and D (Figs 8–10). These specimens were essentially characterized by the existence of iron nanoparticles ranging from 1 to 20 nm in diameter. The isothermal magnetization versus applied magnetic field curves had an entirely different aspect from those of specimen A. The magnetic behaviour was also strongly a function of the temperature.

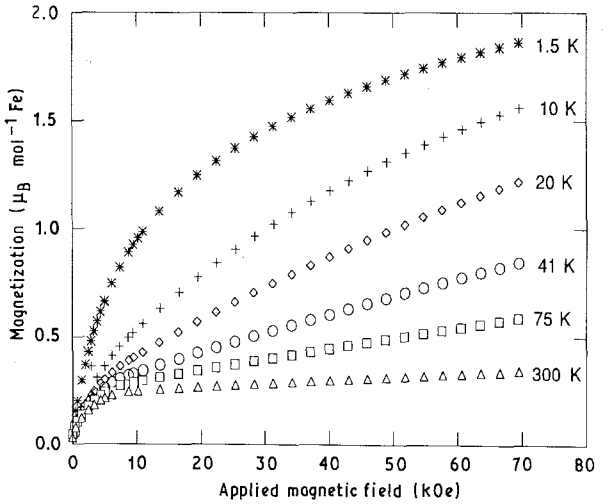

Figure 8 Isothermal magnetization versus applied magnetic field curves for specimen B: (*) 1.5 K, (+) 10 K, (◇) 20 K, (○) 41 K, (□) 75 K and (△) 300 K. 1 Oe ≈ 79.58 A m^{-1}; 1 $\mu_B \approx 9.27 \times 10^{-24}$ J T^{-1}.

For temperatures below 10 K the magnetization curves showed superparamagnetic behaviour. It was not possible to obtain saturation in a 70 kOe field at

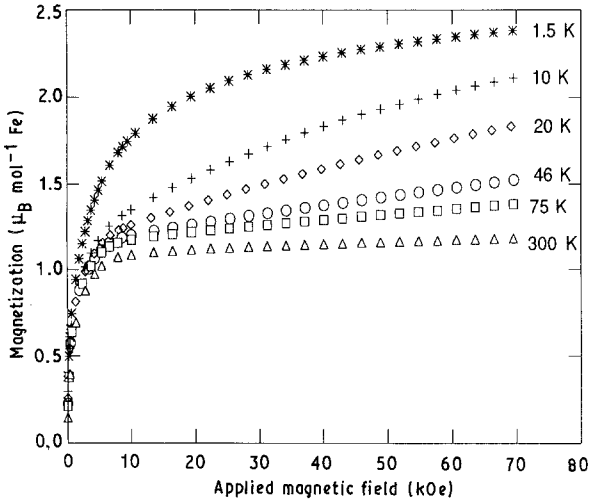

Figure 9 Isothermal magnetization versus applied magnetic field curves for specimen C: (✳) 1.5 K, (+) 10 K, (◇) 20 K, (○) 46 K, (□) 75 K and (△) 300 K 1 Oe ≈ 79.58 A m^{-1}; 1 $\mu_B \approx 9.27 \times 10^{-24}$ J T^{-1}.

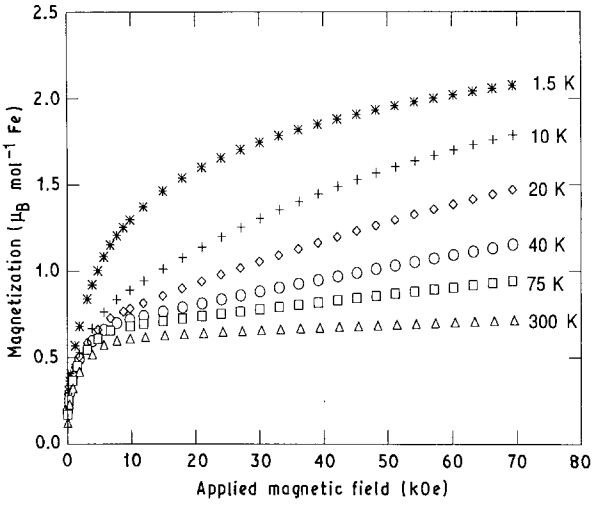

Figure 10 Isothermal magnetization versus applied magnetic field curves for specimen D: (✳) 1.5 K, (+) 10 K, (◇) 20 K, (○) 40 K, (□) 75 K and (△) 300 K 1 Oe ≈ 79.58 A m^{-1}; 1 $\mu_B \approx 9.27 \times 10^{-24}$ J T^{-1}.

1.5 K. Moreover, saturation magnetization was not obtained in a 200 kOe field at 4.2 K. We evaluated the saturation magnetization by linear extrapolation of the M $(1/H^2)$ law at 1.5 K; the values obtained are given in Table III. It is interesting to note that the sample surrounded by antiferromagnetic aluminate had a smaller saturation moment.

For temperatures between 40 and 300 K, when the magnetic field was > 50 kOe at 40 K, > 20 kOe above 300 K, magnetization increased linearly with the applied magnetic field. In this temperature range isothermal magnetization might be expressed as

$$M = M_{sp} + \chi H$$

We report the $M_{sp}(T)$ values for these three specimens in Fig. 11. The superposed susceptibilities follow a Curie–Weiss law. The effective moments had the values 4.76 μ_B mol^{-1} iron for specimen B, 4.41 for specimen C and 4.64 for specimen D.

For temperatures between 10 and 35 K the temperature domain is a transition domain. In the vicinity of

TABLE III Saturation magnetization (M_{sat}) determinated by $1/H^2$ extrapolation law, spontaneous magnetization (M_{sp}) obtained by extrapolation at 0 K of measured magnetization between 40 and 300 K (Fig. 11) and Curie constant, obtained from superposed susceptibility between 40 and 300 K

Specimen	M_{sat} at 1.5 K ($\pm$ 0.03 μ_B)	M_{sp} ($\pm$ 0.02 μ_B)	Curie constant (e.m.u. mol^{-1})
A	2.21	2.17	
B	2.04	0.26	2.83
C	2.50	1.18	2.43
D	2.24	0.67	2.69

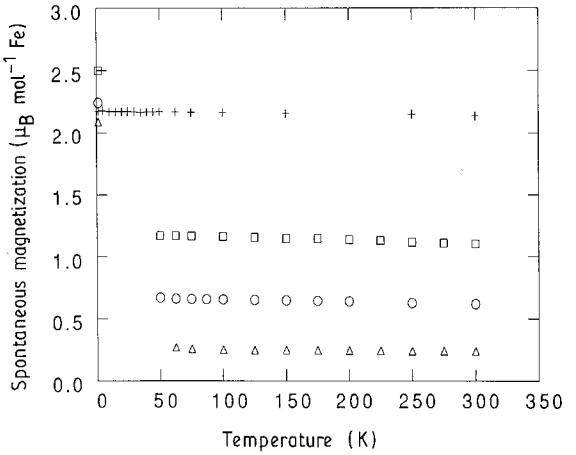

Figure 11 Spontaneous magnetization curves versus temperature from 50 to 300 K for specimens B (△), C (□) and D (○) and from 1.5 to 300 K for specimen A (+). The saturation magnetization at 1.5 K is given for specimens B, C and D. 1 $\mu_B \approx 9.27 \times 10^{-24}$ J T^{-1}.

10 K, for magnetic fields < 15 kOe, the isothermal magnetization curves were similar to those obtained at low temperatures. In high magnetic fields the behaviour of the magnetization versus magnetic field became linear. However, this linearity began at progressively lower magnetic field as the temperature increased (curves at 15, 20 and 30 K). Isotherms at 30 and 35 K showed the same behaviour as isotherms for temperatures > 40 K.

3.3.2. Remanent magnetization versus temperature

Thermomagnetic analysis by means of remanence versus temperature curves brought out two different types of behaviour for specimen A, on the one hand, and for specimens B, C and D, on the other hand (Fig. 12). In the case of specimen A, the remanent magnetization was small and decreased slightly when the temperature increased. For specimens B, C and D we observed essentially two domains of temperature, one from 1.5 to 10 K where the remanent magnetization varied very quickly with temperature and the second above 50 K where the variation was smooth. It could be expected that the remanent magnetization would be higher, the smaller the mean particle sizes. However, this was true only for particles of average size < 10 nm.

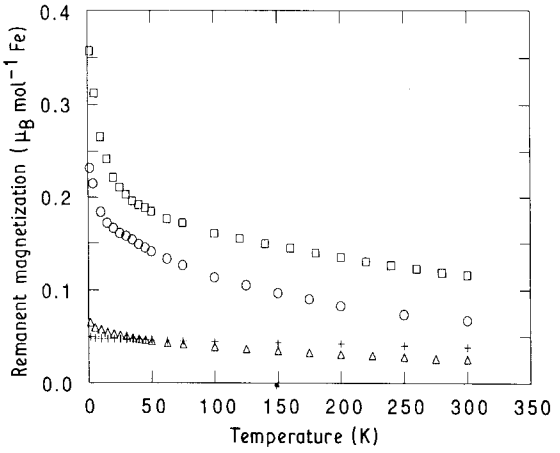

Figure 12 Remanent magnetization curves versus temperature for specimens A (+), B (△), C (□) and D (○). 1 $\mu_B \approx 9.27 \times 10^{-24}$ J T^{-1}.

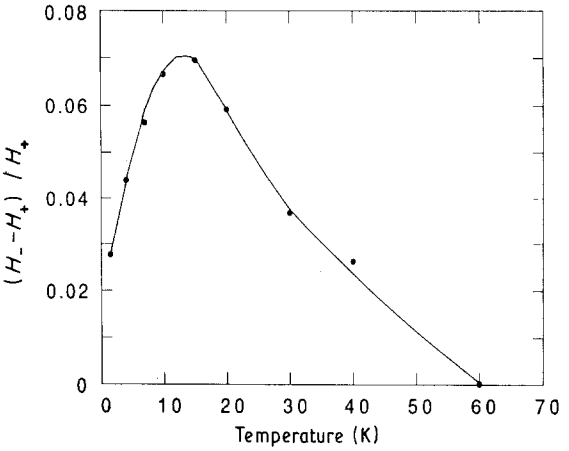

Figure 14 Comparison between values of negative and positive coercive fields following temperature for specimen B 10%.

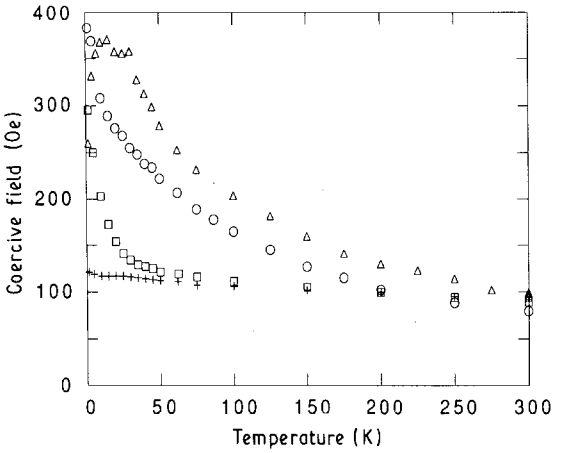

Figure 13 Evolution of coercive field following the temperature for specimens A (+), B (△), C (□) and D (○). 1 Oe ≈ 79.58 A m^{-1}.

TABLE IV For specimen B (10%), coercive fields H_+ when field increases and coercive fields $H_-(i)$ when field decreases at the ith cycle

T (K)	H_+ (Oe)[a]	H_- (1) (Oe)	H_- (2) (Oe)	H_- (3) (Oe)
1.5	253	260	255	255
4	318	332	328	323
7	337	356	353	352
10	345	368	360	359
15	345	369	362	361
20	338	358	356	353
30	326	338	333	333
40	305	313	312	312
100	197	198	198	197

[a] 1 Oe ≈ 79.58 A m^{-1}.

TABLE V For specimen B (5%), coercive fields H_+ when field increases and coercive fields $H_-(i)$ when field decreases at the ith cycle

T (K)	H_+ (Oe)[a]	H_- (1) (Oe)	H_- (2) (Oe)	H_- (3) (Oe)
1.5	101	118	116	117
4	196	240	226	221
10	352	421	389	380
30	515	541	534	531
40	498	516	515	515

[a] 1 Oe ≈ 79.58 A m^{-1}.

3.3.3. Coercive fields and hysteresis loops

Table IV and Fig. 13 show the results of the determination of coercive fields measured at different temperatures. In the case of specimen A, the coercive field increased very slowly from 100 to 125 Oe when the temperature was decreased from 300 to 1.5 K. In the case of specimens B, C and D the increase in the coercive field was rapid below 60 K. In the case of specimen B we observed, in addition to this behaviour, a decrease in the coercive field from 20 to 1.5 K. For this latter specimen, hysteresis loops were highly dissymmetrical below 50 K. When the applied magnetic field decreased from 70 to − 70 kOe, we determined the coercive field H_- [H_- values are given in Fig. 13 and these values are also the H_- (1) values given in Table IV]. When the applied magnetic field increased from − 70 to 70 kOe, we determined the coercive field H_+. A plot of $(H_- - H_+)/H_+$ versus temperature is given in Fig. 14. This difference began to be significant below 40 K. When we plotted successive hysteresis loops at the same temperature, the coercive field H_+ remained constant whereas H_- decreased during the first three loops and afterwards became constant but remained greater than H_+ (Table IV). These phenomena are much more important in the case of specimen B 5% containing only 5% iron [24]. Results corresponding to the decrease in the coercive field H_- during successive hysteresis loops are given in Table V for specimen B 5%. The asymmetry of the hysteresis loop is shown in Fig. 15.

3.3.4. Thermomagnetic evolution and thermoremanence

We realized for these materials the two following experimental procedures.

First procedure:

cooling with no applied field from 300 down to 4 K;

application of a 70 kOe magnetic field;

cancelling of the magnetic field;

magnetization measurements for no magnetic

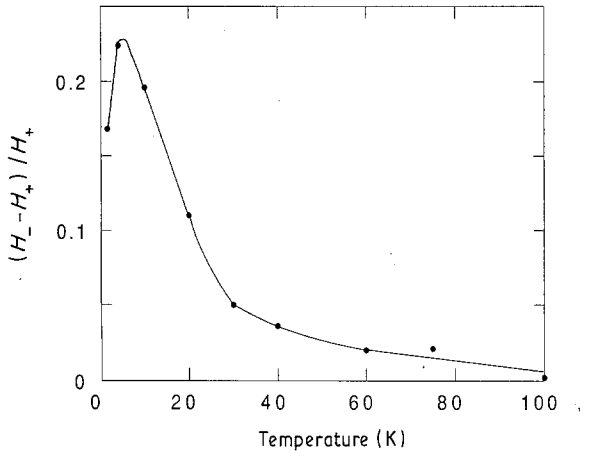

Figure 15 Comparison between values of negative and positive coercive fields following temperature for specimen B 5%.

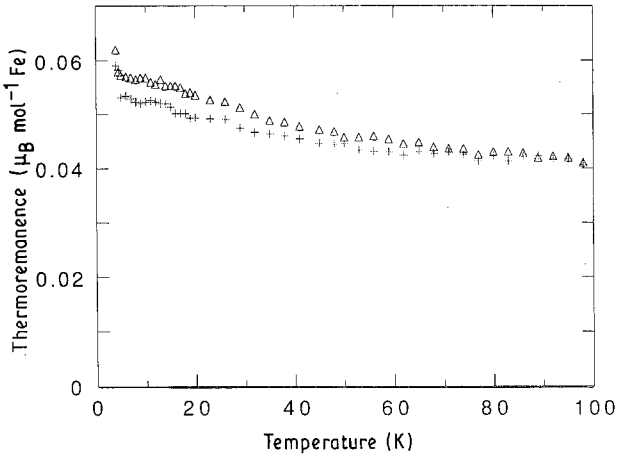

Figure 16 Evolution of thermoremanence following temperature for different processes (see the text) in the case of specimen B 10%: (+) procedure 1 and (△) procedure 2. 1 $\mu_B \approx 9.27 \times 10^{-24}$ J T^{-1}.

field from 4 up to 300 K.

Second procedure:

cooling with a 70 kOe magnetic field from 300 down to 4 K;

cancelling of the magnetic field;

magnetization measurement for no magnetic field from 4 down to 300 K.

In the case of specimens A, C and D, magnetization versus temperature curves merged for the two procedures with curves given in Fig. 12 (remanent magnetization is determinated from the hysteresis loop). The results for specimen B are shown in Fig. 16. The two curves showed a sizeable difference for low temperatures. The relative difference was about 5% between 40 and 70 K. Above 70 K the curves obtained from these two procedures merged. As for the shift in the coercive field, this phenomenon was much more important for the specimen containing only 5% iron (Fig. 17).

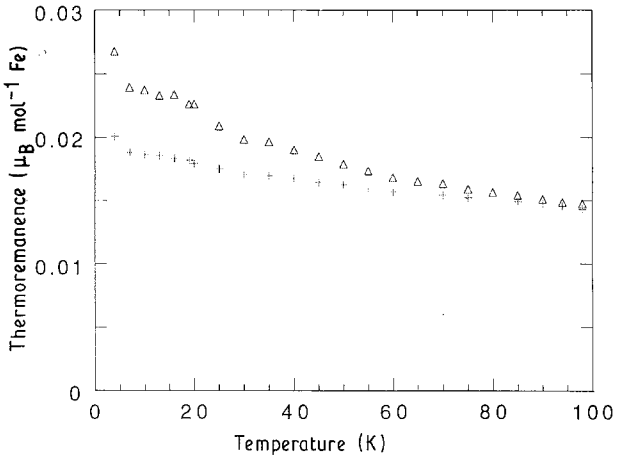

Figure 17 Evolution of thermoremanence following temperature for the same processes as Fig. 12 for specimen B 5%: (+) procedure 1 and (△) procedure 2. 1 $\mu_B \approx 9.27 \times 10^{-24}$ J T^{-1}.

4. Analysis of the results

The behaviour of isothermal magnetization versus applied magnetic field (Figs. 6–10) and of remanent magnetization versus temperature curves (Fig. 12) showed that the magnetic phase of large ferromagnetic particles is also present as a fraction of the total sample in the three other materials. This phase is ferromagnetic between 1.5 and 300 K. The magnetization of this phase (M_{sp}) is reported in Fig. 11 for all samples. These values, extrapolated to 0 K give logically 2.21 μ_B mol^{-1} iron in the case of specimen A. However, for specimens B, C and D the extrapolated values varied from 0.26 to 1.18 μ_B mol^{-1} iron, determined from the total mass of iron in the material. This means that the weight percentage of iron in the ferromagnetic state varied for these three materials from 12 to 47%, if we assume that iron is totally in the metallic state (interfacial Fe^{3+} is possible but not very important in a 10% sample). A second phase existed in materials B, C and D; this phase was paramagnetic above about 40 K and ferromagnetic at lower temperatures. This last magnetic phase was due to iron nanoparticles of size from 1 to 4 nm. These nanoparticles were superparamagnetic with blocking temperatures that were a function of their diameter. The distribution of blocking temperature ranged from a few to some tens of kelvin, as is seen from the slow transition versus temperature of magnetization isothermal behaviour (Figs. 8–10) and remanent magnetization (Fig. 12) between about 10 and about 40 K. These particles having a superparamagnetic behaviour above their blocking temperatures, we determined their effective moment from their reciprocal susceptibility ($1/\chi$) versus temperature curves (Table III). It is important to remark that the values of the effective moments (4.76, 4.41 and 4.64 μ_B for specimens B, C and D, respectively) do not take into account that a large fraction of the iron was already saturated in fields < 5 kOe. This fraction was (Figs 8–10) 0.35 μ_B for specimen B, 1.1 μ_B for specimen C and 0.6 μ_B for specimen D, giving an iron fraction number which does not participate to the Curie constant of, respectively, 0.25/2.04, 1.1/2.50 and 0.6/2.24. The effective superparamagnetic moments were therefore 4.76/0.877 = 5.42 μ_B for specimen B, 4.41/0.56 = 7.87 μ_B for specimen C and 4.64/0.73 = 6.33 μ_B for specimen D.

The mean particle sizes deduced from these values were 6, 13 and 8.27 iron mole. These correspond to an average particle diameter of 0.7 nm. These numbers are smaller than those given in Table III for two reasons: first, the larger particles of the distribution in Table III and not here, and secondly, this evaluation of particle size is a simple average. It is important to take into account the whole distribution [25–27].

The coercive field in specimen A varied slowly between 300 and 1.5 K. It was characterized by competing dipolar interaction between particles of diameter extending from 50 to 100 nm. For the three other specimens the coercive field increased strongly when the temperature decreased. Below the blocking temperature the coercive field of superparamagnetic particles was larger than to that of the bulk iron material [5]. However, this effect was modified at very low temperatures in the case of specimens B 10% (and B 5%) for which a rather thick shell of antiferromagnetic iron aluminate surrounded iron nanoparticles. These iron aluminate shells were about 2.5 nm thick. They behaved like a superantiferromagnet coupled with a bulk superferromagnet. The shell non-compensated moment is parallel to the antiferromagnetic axis of each particle [28]. Above the antiferromagnetic blocking temperature this moment can easily reverse. When an exterior magnetic field was applied at a temperature above this blocking temperature (procedure 2, Figs 16 and 17), a certain number of moments of this antiferromagnetic phase became parallel to the magnetic field, and during cooling these moments remained parallel to the applied field. Then the antiferromagnetic shell gave a magnetic moment parallel to the bulk particle ferromagnetic moment and then contributed to remanence (Fig. 16). If the field was applied below the blocking temperature it did not modify the antiferromagnetic structure unless extremely large. In this case the remanent magnetization must be smaller (Fig. 16). However, the blocking temperature of the superantiferromagnetic phase must be lower than the Néel temperature of the massive phase (for pure $FeAl_2O_4$ $T_N = 8$ K [29]). In this case we observed that the blocking temperature of the superantiferromagnetic phase was about 60 K. We conclude that the interfacial phase is not pure iron aluminate, but a solid solution of magnetic and hercynite [30].

This coupling between the bulk iron particles and magnetite/hercinyte antiferromagnetic shell also induced a dissymmetry of the hysteresis loops and a shift of coercive field as observed in Figs 14 and 15 and Tables IV and V. In effect, reversal of iron moments during hysteresis loops modified the spinel magnetization at its surface. As this modification was induced during iron moments reversal, the spinel magnetic moments must decrease. Consequently, the coercive field H_- must decrease slightly (Table IV for specimen B 10% and Table V for specimen B 5%), but this effect cannot reach very deeply into the iron aluminate layer, so there is a persistent asymmetry of hysteresis loops after three loops.

These phenomena, due to the existence of a antiferromagnetic spinel shell, should be more important if the quantity of iron in the spinel layer is greater than in the metal nanoparticle. This was the case in specimen B 5%, which contained less iron than and the same order of aluminate as specimen B 10%. This explains the difference between the results given in Tables IV and V, and the fact that the different effects due to the presence of this aluminate were much more pronounced in specimen B 5% than in specimen B 10%. Identical phenomena were first observed by Meiklejohn and Bean [31, 32] in a compact of fine particles of cobalt (10–100 nm) which had a cobaltous oxide coating.

The saturation magnetization for 1 mol iron was 2.21 μ_B for specimen A. This value, close to that in bulk iron, is due to the large average size of the iron particles, any interfacial modification being negligible with respect to the particle bulk magnetization. In the case of specimen B, we found only 2.04 μ_B for the saturation magnetization. Indeed, the aluminate layer did not contribute much to the magnetization. In the case of specimen D (specimen B after reduction) we found the value 2.24 μ_B, again close to that of bulk iron. However, for specimen C the saturation magnetization, 2.50 μ_B, was larger than the value for bulk iron. This might be due to a modification of the electronic structure of metallic iron atoms at the particles surface [10] and the existence of iron atoms with a magnetic moment > 2.22 μ_B and able to reach 2.6 or 2.7 μ_B. In our case it seems more plausible to envisage the existence at the iron–alumina interface of one or two layers of ionic iron (Fe^{2+} and/or Fe^{3+} with moment of 4/5 μ_B). Because of the conditions of material preparation, the existence of Fe^{2+} is unlikely.

References

1. L. NÉEL, *C.R. Hebd. Séanc. Acad. Sci. Paris* **228** (1949) 664.
2. L. NÉEL, *Ann. Geophys.* **5** (1949) 99.
3. C. P. BEAN, *J. Appl. Phys.* **26** (1955) 1381.
4. C. KITTEL, *Phys. Rev.* **70** (1946) 965.
5. I. S. JACOBS and C. P. BEAN, in "Magnetism III", edited by G. T. Rado and H. Suhl (Academic Press, New York, 1963) p. 271.
6. J. L. DORMANN, *Revue Phys. Appl.* **16** (1981) 275.
7. P. W. SELWOOD, "Adsorption and Collective Paramagnetism" (Academic Press, New York, 1962).
8. G. A. MARTIN, N. CEAPHALAU, P. DE MONTGOLFIER and B. IMELIK, *J. Chim. Phys.* **70** (1973) 1422.
9. J. T. RICHARDSON, *J. Appl. Phys.* **49** (1978) 1781.
10. A. J. FREEMAN and C. L. FU, *ibid.* **61** (1987) 3356.
11. L. N. LIBERMANN, D. R. FREDKIN and H. B. SHORE, *Phys. Rev. Lett.* **22** (1969) 539.
12. L. N. LIBERMANN, J. CLINTON, P. M. EDARDS and J. MATHON, *ibid.* **25** (1970) 232.
13. S. OHNISHI, A. J. FREEMAN and M. WEINERT, *Phys. Rev.* **B28** (1983) 6741.
14. G. M. PASTOR, J. DORANTE-DAVILA and K. M. BENNEMAN, *ibid.* **B40** (1989) 7642.
15. S. MATSUO and I. J. NISHIDA, *Phys. Soc. Jpn.* **49** (1980) 1005.
16. A. ROUSSET and X. DEVAUX, French Patent 90 09790 (1990).
17. J. A. IMLACH and F. P. GLASSER, *Trans. J. Brit. Ceram. Soc.* **70** (1971) 227.
18. S. B. OGALE, D. M. PHASE, S. M. CHAUDARI, S. V. GHAISAS, S. M. KANETKAR, P. P. PATIL, V. G. BHIDE and S. K. DATE, *Phys. Rev.* **B35** (1987) 1593.

19. R. ANTON, K. HEINEMANN and H. POPPA, *Vide Couches Minces* **201** (1980) 121.
20. S. B. QADRI, J. H. CLAASSEN, P. R. BROUSSARD and S. A. WOLF, *J. Less-Common Metals* **155** (1989) 327.
21. J. P. REBOUILLAT, Thèse d'Etat, Université de Grenoble (1972).
22. J. H. M. STOELINGA, R. GERSDORF and G. DE VRIES, *Physica* **41** (1969) 457.
23. S. FONER, A. J. FREEMAN, N. A. BLUM, R. B. FRANKEL, E. J. MCNIFF and H. C. PRADDANDE, *Phys. Rev.* **181** (1969) 863.
24. A. MARCHAND, X. DEVAUX, B. BARBARA, P. MOLLARD and A. ROUSSET, to be published.
25. B. BARBARA, J. FILIPPI, A. MARCHAND, P. MOLLARD, X. DEVAUX and A. ROUSSET, *J. Phys., Paris* **2** (1992) 101.
26. B. BARBARA, A. MARCHAND, P. MOLLARD, X. DEVAUX and A. ROUSSET, in International Workshop on Studies of Magnetic Properties of Fine Particles and Their Relevance to Materials Science, Rome, 4–8 November, 1991.
27. *Idem*, to be published.
28. L. NÉEL, *Ann. Phys.* **2** (1967) 61.
29. W. L. RUTH, *J. Phys., Paris* **25** (1964) 507.
30. S. J. PICKARD and A. C. TURNOCK, *Phys. Chem. Solids* **10** (1959) 242.
31. W. H. MEIKLEJOHN and C. P. BEAN, *Phys. Rev.* **102** (1956) 1413.
32. *Idem, ibid.* **105** (1957) 904.

Received 16 December 1991
and accepted 2 September 1992